Etching Process Effects on Surface Structure, Fracture Strength, and Reliability of Single-Crystal Silicon Theta-Like Specimens

Michael S. Gaither, Richard S. Gates, Rebecca Kirkpatrick, Robert F. Cook, and Frank W. DelRio

***Abstract*—The etching processes used to produce microelectromechanical systems (MEMS) leave residual surface features that typically limit device strength and, consequently, device lifetime and reliability. In order to optimize MEMS device reliability, it is therefore necessary to determine the effects that these etching processes have on MEMS component strength. The microscale theta specimen, which is shaped like the Greek letter Θ, acts as a tensile test specimen when loaded in compression by generating a uniform tensile stress in the central web region of the specimen. Three sets of single-crystal silicon theta specimens are fabricated using two deep reactive ion etching recipes and a temperature–controlled cryogenic plasma etching recipe, each set resulting in a different specimen surface structure. The resulting strength distributions are analyzed in two ways. First, the strength data are fit to a three-parameter Weibull distribution function to determine the lower bound, or threshold strength, of each distribution. Second, the strength data are used in conjunction with various loading schemes to assess their effect on the lifetime spectrum of the device. In both approaches, the theta specimen is used to great effect to gain quantitative insight into the role of etching-induced surface features on the manufacturing yield and operational reliability of MEMS components. [2012-0302]**

***Index Terms*—Materials testing, microelectromechanical systems (MEMS), reliability, silicon, stress measurement.**

I. Introduction

MICROELECTROMECHANICAL systems (MEMS) have numerous applications, from noncontacting sensors such as accelerometers, gyroscopes, and pressure gauges, to more complicated devices with contacting and rubbing components—one of the few such devices to be commercially viable to date is the digital mirror array used in high-brightness displays [1]. A major factor inhibiting the commercialization of devices in the latter category is that of uncertain mechanical reliability. In particular, surface phenomena such as adhesion [2], [3] and friction [4], [5] contribute to the uncertainty and become increasingly dominant at small length scales due to the large surface-to-volume ratios, small surface separations, and highly compliant components. Such phenomena not only hinder relative motion at interfacial contacts but also impose a lower bound on the fracture strength, or threshold strength, of the components [6]. This strength constraint requires MEMS designers and manufacturers to either optimize their fabrication methods or component geometry, such that the maximum stress in the component never exceeds the threshold strength, or, if this is not possible, to characterize the full set of parameters describing the strength distribution of a constrained fabrication method, thereby providing probabilistic insight into the likelihood that some components will fail prior to the desired lifetime.

Regardless of the approach, it is clear that the development and optimization of microscale devices subject to mechanical forces is greatly dependent on mechanical properties measurements at small length scales. However, mechanical testing at small length scales is difficult [7]: Not only are the involved loads and displacements small, making measurement difficult, but issues of specimen gripping and loading alignment, which are also often problematic at large scales, are more difficult as well. In addition, posttest sample collection and manipulation are taxing, which impedes the ability to identify property-limiting structural defects during failure analysis and thus hinders the development of processing–structure–mechanical properties linkages. To address this measurement need, a number of test structures have been developed to measure the strength of MEMS materials, most of which attempt to replicate large-scale tensile test specimen geometries, such as tensile bars [8], fixed–free [9] and fixed–fixed beams [10], and biaxial flexure plates [11]. Because of the aforementioned difficulties with mechanical testing at small length scales, these studies were typically limited to small data sets, hindering their ability to accurately describe the lower tail of strength distributions. Other test specimens that have enabled statistically meaningful numbers of small-scale tensile strength measurements have often employed more complex geometries microfabricated from a multilayer polycrystalline Si material; these included "pull-tab" [12] and "slack-chain" [13] designs, for which specialized mechanical loading systems were required, and "on-chip" [14] devices, for which electrical connection was required for thermal actuation of the tests.

Recently, a new experimental test specimen that allows the fracture strength of brittle materials to be measured at small

Manuscript received October 16, 2012; revised December 6, 2012; accepted December 9, 2012. Date of publication January 18, 2013; date of current version May 29, 2013. Subject Editor J. A. Yeh.

M. Gaither, R. Gates, R. Cook, and F. DelRio are with the Materials Measurement Science Division, Material Measurement Laboratory, National Institute of Standards and Technology, Gaithersburg, MD 20899 USA (e-mail: michael.gaither@nist.gov; richard.gates@nist.gov; robert.cook@nist.gov; frank.delrio@nist.gov).

R. Kirkpatrick is with the Materials Measurement Science Division, Material Measurement Laboratory, National Institute of Standards and Technology, Gaithersburg, MD 20899 USA, and also with The Pennsylvania State University, University Park, PA 16802 USA (e-mail: rebecca.kirkpatrick@nist.gov).

Color versions of one or more of the figures in this paper are available online at http://ieeexplore.ieee.org.

Digital Object Identifier 10.1109/JMEMS.2012.2234724

scales has been introduced [15], [16]. The test specimen does not attempt to replicate large-scale tensile test specimen geometries with the attendant gripping and alignment difficulties but, instead, integrates the "specimen" into a test "frame." The integrated circular frame and specimen crosspiece, or "web" segment, resembles the Greek letter Θ, and the overall specimen is known as a "theta" specimen [17]. In more recent work, a new theta test specimen that improved on many aspects of the original concept has been presented [18]. Both the original Durelli and new arch geometries were later used to assess the effects of processing variations on strength, albeit in an *unintended* demonstration [19]. Here, we extend the usage of the theta test specimen to examine *intended* and *unintended* etching process effects on surface structure, fracture strength, and reliability of single-crystal silicon. More specifically, three different sets of single-crystal silicon theta specimens are fabricated using two deep reactive ion etching (DRIE) recipes and one temperature-controlled cryogenic plasma etching recipe, each set resulting in a different specimen surface quality. The testing protocol allows many measurements to be performed in a time-effective manner, enabling statistically relevant numbers of strength measurements to be obtained and, thus, an accurate evaluation of the threshold strength and the related processing–structure–property relations. In conjunction with an assumed loading spectrum, it is also shown that the theta test specimen can be used to assess lifetime spectra and form the associated property–performance predictions.

II. Experimental Methods

A. Specimen Design and Fabrication

Both the Durelli and arch theta geometries are formed from a frame with a circular exterior that is attached to a macroscale strip at the base, include a hat structure at the top, and incorporate a web across the center of the specimen. Briefly, the Durelli geometry is based on a design by Durelli *et al.* [17] and consists of three straight sections linked by tangential radii to define the frame interior, whereas the arch theta design consists of a single circular arch to define the frame interior; replacing the complex internal geometry of the Durelli design with a single arch reduces the size and the extent of secondary, nonweb, stresses on loading [18], [19]. The top-hat structure is included to minimize loading misalignments and stress concentrations, which lead to stress gradients across the web region and large secondary stresses outside of the web region, respectively [16]. Both designs use tangential circular sections to incorporate the web and have the same diameter D of 250 μm and web width w of 8 μm.

Fig. 1 shows the fabrication sequence for the theta test samples. Test samples were formed from three different 100-mm-diameter (001) silicon-on-insulator (SOI) wafers, as shown in Fig. 1(a); the test samples resulting from each of these wafers are henceforth referred to as batches A, B, and C. The single-crystal Si device layers were 25.0 ± 0.5 μm thick for batches A and B and 25 ± 1 μm thick for batch C. The SiO_2 insulator layers were 2.0 ± 0.1 μm thick for batches A and C and 1.00 ± 0.05 μm thick for batch B. The Si handle

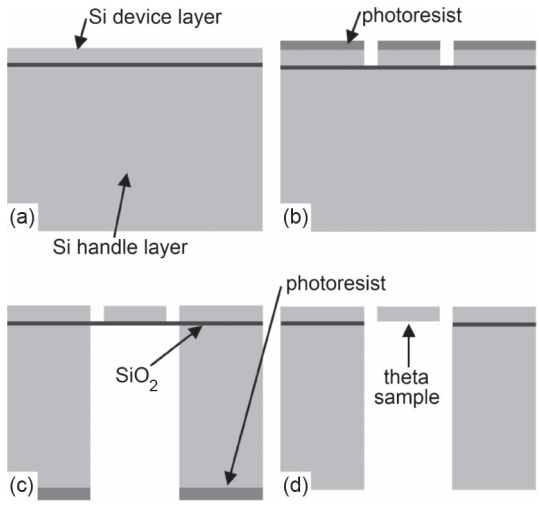

Fig. 1. Fabrication sequence for the theta test samples. (a) The process began with an SOI wafer. (b) The Si device layer and (c) the Si handle wafer were patterned by a photolithographic mask and etched using DRIE to define the device features. (d) The SiO_2 layer was then locally removed with a buffered-oxide etching solution to create the freestanding structures.

layers were 400 ± 10, 400 ± 5, and 480 ± 10 μm thick for the A, B, and C batches, respectively. The preceding uncertainty values correspond to variations across the wafer, as specified by the manufacturer; calibrated field-emission scanning electron microscopy (FESEM) measurements were used to confirm that the layer thicknesses were within the reported tolerances. Each SOI wafer was cleaned with the Radio Corporation of America (RCA) process [20]. In this process, the wafers were subjected to an RCA-1 clean (1:1:5 solution of NH_4OH:H_2O_2:H_2O by volume at 80 °C) for 10 min to remove organic contaminants, an HF clean (1:50 solution of 49% HF:H_2O by volume at 25 °C) for 20 s to remove the thin native oxide layer, and an RCA-2 clean (1:1:5 solution of HCl:H_2O_2:H_2O by volume at 80 °C) for 10 min to remove metallic contaminants. After each cleaning step, the wafers were rinsed with deionized (DI) water for 5 min. After the final rinse, the wafers were placed in a spin rinse dryer tool (SRD-880S31EML, Semitool, Kalispell, MT) to dry the wafer without residue.

The Si device layers were coated with a hexamethyldisilazene (HMDS) adhesion layer (J.T. Baker, Mallinkrodt Baker, Inc., Phillipsburg, NJ) followed by a photoresist film (Microposit S1813, Rohm and Haas Electronic Materials LLC, Marlborough, MA) and then soft-baked on a hotplate at 115 °C for 60 s. The photoresist film was subsequently exposed through a chrome-on-soda-lime glass photolithographic mask using a Suss MicroTec MA8 contact aligner (Munchen, Germany) with a 950-W broadband UV Hg lamp and a total dose of 130 mJ · cm^{-2}, which is aligned such that the web segment of the theta test structures was oriented along a $\langle 110 \rangle$ direction with an estimated misalignment of less than 0.5°. After exposure, the wafers were immersed in Microposit MF-319 (Rohm and Hass Electronic Materials LLC, Marlborough, MA) for 60 s to develop the photoresist, rinsed with DI water for 60 s, dried under a stream of N_2, and hard-baked at 60 °C in a vacuum oven overnight. After a 60-s descum process (15.0-sccm O_2 at a chamber pressure of 80 Pa and a bias power of 150 W) to

improve the sidewall profile of the photoresist, the Si device layers were etched using DRIE to define the sample features, as shown in Fig. 1(b). Each SOI wafer was etched using a different process, which was optimized to produce vertical device sidewalls, most importantly in the web region. The device layers for batches A and B were etched using Bosch DRIE recipes on a deep silicon etching tool (Shuttleline, Unaxis USA Inc, St. Petersburg, FL) with an inductively coupled plasma (ICP) power of 900 W, 40-sccm Ar, and He backside cooling. The Bosch DRIE process alternates between a C_4F_8 passivation step and an SF_6 isotropic etching step, at ambient temperature, to produce an essentially anisotropic etch overall with characteristic etch steps called "scallops" [21], as demonstrated in Fig. 2(a). For the passivation step, both recipes used 60-sccm C_4F_8, the batch A recipe for 2 s at 2.9-Pa chamber pressure and the batch B recipe for 3 s at 3.1 Pa. For the first etch step, which was used primarily to etch through the C_4F_8 film, both recipes used 60-sccm SF_6 and a bias power of 12 W, the batch A recipe for 3 s at 3.2-Pa chamber pressure and the batch B recipe for 4 s at 2.9 Pa. For the second etch step, which etched the silicon, both recipes used a bias power of 12 W at 3.1-Pa chamber pressure, the batch A recipe with 80-sccm SF_6 for 3 s and the batch B recipe with 120-sccm SF_6 for 6 s. To etch through the entire Si device layer of each batch, 80 loops were used with batch A, and 43 loops were used with batch B, both including overetching loops to ensure a completed etch. The etch process for batch B was split into multiple steps to minimize wafer heating and the associated etch nonuniformities. The device layer for batch C was etched using a cryogenic DRIE process on an ICP etching tool (Plasmalab System 100, Oxford Instruments, Bristol, England). The cryogenic DRIE process uses continuous O_2 passivation and SF_6 etching, at $-110\ ^\circ C$, to fabricate high-aspect-ratio structures with relatively smooth sidewall surfaces [22]; a schematic of the process flow is shown in Fig. 2(b). The optimized process started with three stabilization steps; in sequence, the steps were as follows: 1) a temperature stabilization step with 1.3-kPa He backside cooling to bring the wafer to $-110\ ^\circ C$; 2) a process gas stabilization step with 25-sccm SF_6, 5-sccm O_2, and 50-sccm Ar at a chamber pressure of 1.1 Pa; and 3) a plasma strike step using an ICP and a bias power of 1800 and 30 W, respectively, with 28-sccm SF_6, 5-sccm O_2, and 25-sccm Ar. In the subsequent etch step, the bias power was reduced to 5 W, and the Ar was removed, which resulted in a silicon etch rate of 25 $\mu m \cdot min^{-1}$, a sidewall angle of 90°, and a silicon-to-photoresist selectivity of greater than 20.

The Si handle layers were also primed with HMDS but subsequently coated with a thicker photoresist film (Megaposit SPR 220-7.0, Rohm and Haas Electronic Materials LLC, Marlborough, MA) and soft-baked on a hotplate at 115 °C for 90 s. The photoresist film was then exposed through a chrome-on-soda-lime glass mask using a Suss MicroTec MA6 contact aligner (Munchen, Germany) with a 1000-W broadband UV Hg lamp and a 470-mJ $\cdot$ cm^{-2} total dose, such that the device layer and handle layer patterns were aligned. After a 2-h wait, the wafers were immersed in Megaposit MF-26A (Rohm and Hass Electronic Materials LLC, Marlborough, MA) for 120 s to develop the photoresist, rinsed with DI water for 60 s,

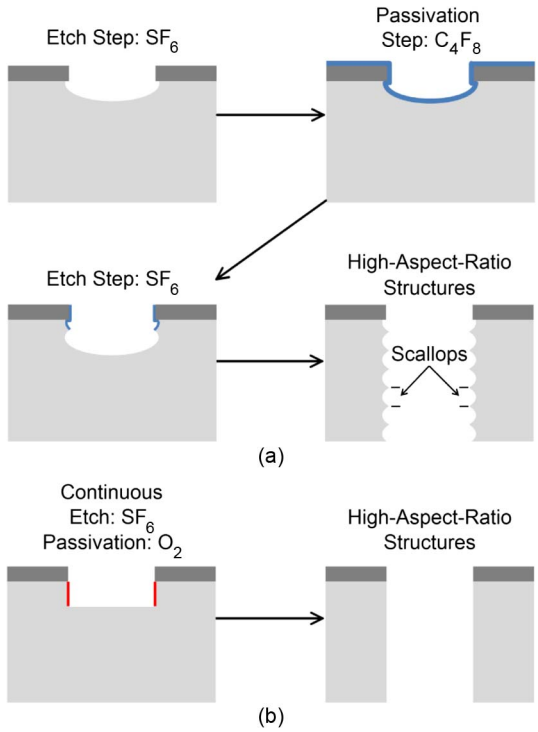

Fig. 2. DRIE processes used to etch the Si device layer and the Si handle wafer. (a) The Bosch DRIE process alternated between a C_4F_8 passivation step and an SF_6 isotropic etching step, whereas (b) the cryogenic DRIE process used continuous O_2 passivation and SF_6 etching.

dried under a N_2 stream, and hard-baked in vacuum at 60 °C. Following the 60- to 120-s descum process, the Si handle layers were etched using DRIE, as shown in Fig. 1(c). All three SOI batches were etched using the same Bosch DRIE process with an ICP power of 900 W, 40-sccm Ar, and He backside cooling. The recipe consisted of a passivation step with 60-sccm C_4F_8 for 3 s, followed by first and second etching steps with 60-sccm SF_6 and a bias power of 12 W for 4 and 7 s, respectively. This three-step process resulted in a Si etch rate of ≈ 1-μm $loop^{-1}$. Hence, 400 loops were required to etch through batches A and B, whereas 480 loops were needed for batch C. The residual photoresist was removed from the device and handle layers using the descum process for 120 s; a photoresist stripper (Microposit Remover 1165, Rohm and Hass Electronic Materials LLC, Marlborough, MA) at 65 °C for 30 min; and microwave ashing (Model 300, PVA TePla, Corona, CA) at 500 W, 60 Pa, and 600-sccm O_2 for 30 min.

After Si etching, the SiO_2 insulator layers were removed with a 6:1 buffered-oxide etch solution (J.T. Baker, Mallinkrodt Baker, Inc., Phillipsburg, NJ) to create the freestanding samples, as shown in Fig. 1(d). Finally, each test strip, consisting of ten Durelli or arch theta samples spaced along a 15-mm length, was removed from the wafer using a diamond scribe on notched regions at each end of the strip.

B. Surface Roughness Characterization and Web Width Determination

The etching processes used to create the theta test specimens enable the *intended* high-aspect-ratio sidewalls but also result

in *unintended* residual surface features that can limit device strength and, consequently, device lifetime and reliability. One of the unintended surface features is surface roughness, or the deviation in the topography of the surface from its ideal counterpart. Here, surface roughness was *qualitatively* examined by inspecting a number of the samples using an Ultra 60 (Carl Zeiss, Thornwood, NY) FESEM with an accelerating voltage of 10 kV and a working distance of ≈6 mm; these samples were sputter coated with gold-palladium and mounted on carbon-taped FESEM stubs prior to examination and, thus, excluded from subsequent measurements or testing. Moreover, surface roughness was *quantitatively* measured on a number of other samples using a Dimension V (Bruker AXS, Santa Barbara, CA) atomic force microscope (AFM). Intermittent-contact mode AFM, at a line scan rate of 1 Hz, was used to scan $5.0\ \mu\text{m} \times 5.0\ \mu\text{m}$ regions of sample sidewall surfaces, using RTESP cantilevers (Bruker AFM Probes, Camarillo, CA) with a nominal 40-$\text{N} \cdot \text{m}^{-1}$ spring constant, a 300-kHz resonance frequency, and a 10-nm tip radius. The resulting surface height h_s data were then used to calculate a number of different surface roughness metrics, including the root-mean-square (RMS) height variation h_{rms}, the peak-to-valley height h_{pv}, and, for samples fabricated with the Bosch DRIE process, the scallop pitch r_{scallop}.

Due to lithographic and DRIE variability across the wafers, variations in web width w were also observed. To quantify the variations, high-contrast optical microscope images for every sample prior to testing were digitally recorded and imported into an image processing program (IGOR Pro, WaveMetrics Inc., Lake Oswego, OR). The minimum and maximum intensity in each image were used to set a half-maximum intensity variation, and a web dimension at each section was defined as the full-width at half-maximum of the intensity variation. The web dimensions from every section in an image were combined to generate a mean and standard deviation web width in pixels for that sample. Such oversampling allowed superresolution subpixel standard deviations to be obtained for the web widths. Calibration of the microscope and the image processing program using a calibrated pitch grating enabled the web width to be converted from pixels to micrometers.

C. Mechanical Testing and Finite-Element Analysis

The test strips were clamped across the full SOI wafer thickness into a fixture that was then mounted into an instrumented indentation testing (IIT) device (Nano Indenter XP, MTS Systems Corporation, Eden Prairie, MN), such that samples were upright and isolated from the surrounding clamp material. Each sample was diametrally compressed *via* IIT using a 250-μm-radius spherical sapphire indenter tip (Micro Star Technologies, Huntsville, TX) and an IIT break-detection routine, which was developed within the IIT software (Testworks v.4.10A, MTS Systems Corporation, Eden Prairie, MN), to withdraw the tip on the detection of sample failure to minimize subsequent sample damage. Two sets of test conditions were used for all samples. In the first set, the IIT device was operated in load control and set to load to a peak load, cycle several times between the peak load and a smaller load, and then unload. In the second, the IIT device was operated at a target displacement rate and loaded until the break-detection routine detected a rapid increase in indenter velocity, which is associated with an increase in sample compliance and sample failure, and withdrew the indenter. Load and displacement were recorded throughout the cyclic loading and sample failure measurements with data acquisition rates of 5 and 100 Hz, respectively. For batch A samples, the indenter tip was removed from sample contact between the two tests, but for batches B and C samples, the tests were combined to perform the complete procedure without unseating the indenter tip, thereby eliminating an intermediate nonlinear response associated with the seating of the tip on the rough etched surface of the hat [18], [19].

Sample load P and displacement h data were converted into the longitudinal stress σ and strain ε in the web region using finite-element analysis (Abaqus, Simulia, Providence, RI). Each specimen simulation utilized more than 100 000 eight-node linear hexahedral mesh elements; the critical specimen web region had 36–66 elements in cross section and approximately 2000–10 000 total elements within the web region, with more elements used for smaller web widths. Silicon orthotropic elastic properties were used and oriented as in the fabrication sequence, aligning $\langle 110 \rangle$ with the theta web axis; the elastic stiffness values were $C_{11} = 165.773$ GPa, $C_{12} = 63.924$ GPa, and $C_{44} = 79.619$ GPa [23]. Simulated loads of 20–200 mN in increments of 20 mN, along with a load of 2 N, were applied to the top center of the theta specimens using a hemisphere with a 250-μm-radius indenter and isotropic elastic property values approximating sapphire with Young's modulus of 400 GPa and Poisson's ratio of 0.24 [24].

In all simulations, σ and ε were linearly related and linearly related to P and h, respectively, through the theta diameter D, web width w, and specimen thickness t_s. In addition, specimen compliance λ was determined by averaging over all simulated loads. The σ and ε relationships for the Durelli and arch theta specimens both maintained the following forms [19]:

$$\sigma = -K_\sigma P/Dt_s \tag{1}$$

$$\varepsilon = -K_\varepsilon h/D \tag{2}$$

$$\lambda = K_\lambda \lambda_I \tag{3}$$

where λ_I is the ideal ($w = 8\ \mu$m) compliance for a given specimen geometry. Equations (1) and (2) include negative signs as P and h were taken in the specimen compressive direction, whereas σ and ε were taken in the web tensile direction. The coefficients K_σ, K_ε, and K_λ were found to be well described by simple inverse dependencies on w, and averaging over several widths for each specimen generated the following expressions:

$$K_{\sigma,D}(w) = 97.224/w + 2.408 \tag{4}$$

$$K_{\varepsilon,D}(w) = 1.660/w + 0.363 \tag{5}$$

$$K_{\lambda,D}(w) = 2.469/w + 0.705 \tag{6}$$

for Durelli theta specimens and

$$K_{\sigma,A}(w) = 86.001/w + 3.751 \tag{7}$$

$$K_{\varepsilon,A}(w) = 1.670/w + 0.439 \tag{8}$$

$$K_{\lambda,A}(w) = 2.309/w + 0.725 \tag{9}$$

for arch theta specimens. In (4)–(9), K_σ, K_ε, and K_λ are dimensionless, and w is in micrometers.

Sample strength σ_f was calculated from the peak load at sample failure and the web width as determined by the image processing program described earlier. The resulting values for σ_f were fit to a three-parameter Weibull distribution function, i.e.,

$$P_f = 1 - \exp\left\{-\left[(\sigma_f - \sigma_{\rm th})/\sigma_\theta\right]^m\right\} \tag{10}$$

where P_f is the cumulative failure probability, m is the Weibull modulus, σ_θ is the scaling strength, and $\sigma_{\rm th}$ is the threshold strength (the "characteristic strength," where $P_f = 0.632$, is $\sigma_c = \sigma_\theta + \sigma_{\rm th}$). P_f was assigned to each strength value by

$$P_f = (i - 0.5)/N \tag{11}$$

where i is the rank of the strength in an ascending-order ranked strength distribution, and N is the number of samples. The Weibull distribution parameters m, σ_θ, and $\sigma_{\rm th}$ were found via least squares fitting based on the Levenberg–Marquardt algorithm. In addition, the strength values were used to estimate the critical flaw size leading to sample failure. The flaw sizes c_s were estimated assuming simple nonresidually stressed flaws, i.e.,

$$c_s = (T/\Psi\sigma_f)^2 \tag{12}$$

where $T = 0.71$ MPa $\cdot$ m$^{1/2}$ is the material toughness for the (110) plane of Si [25], and $\Psi = 1.12\pi^{1/2}$ is the crack geometry term for a sharp edge crack on a planar surface [26]. For the surfaces here, which exhibit nanoscale roughness, as shown in the succeeding discussion, (12) is extended to represent the flaw as a sharp crack of length c_f at the bottom of a semielliptical notch of depth a. In this case, the relation between strength and size is given by (12) with [27]

$$c_f = c_s - a. \tag{13}$$

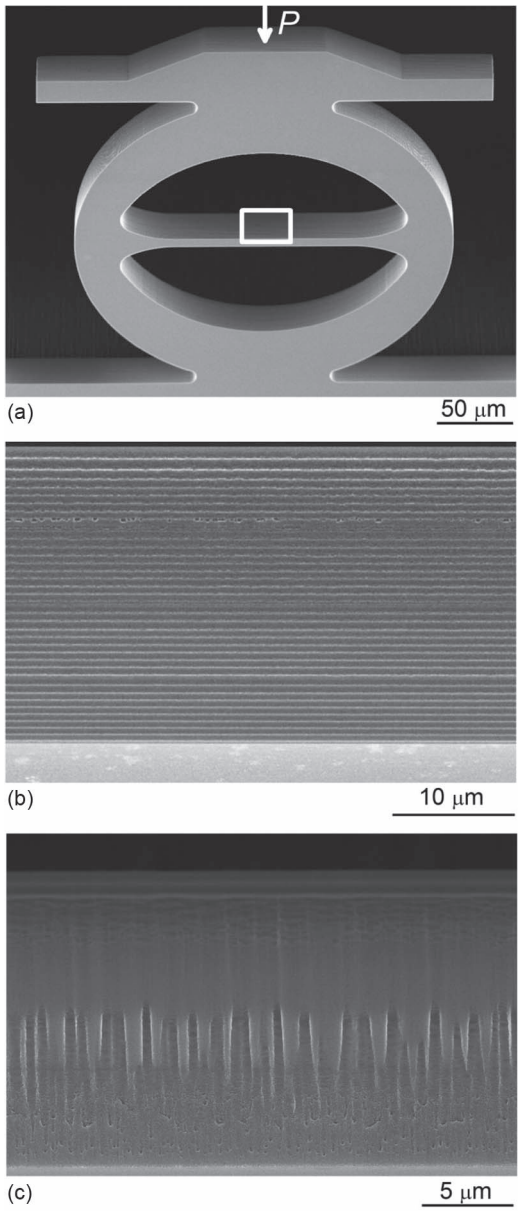

Fig. 3. FESEM images of the sidewall etch surfaces. A portion of the web region is indicated by the box in the tilted theta sample of (a). In (b) and (c), the etch process started at the bottom and progressed to the top. In (b), the surface consists of regular etch scallops, characteristic of the Bosch DRIE process, across the thickness of the web region. In (c), the cryogenic DRIE surface is initially smooth relative to Bosch DRIE scallops but degrades in the latter stages of the etch as the edges of the photoresist degrade.

III. Results

A. Surface Structure

Fig. 3(a) shows a FESEM image of a completed arch theta test sample. In previous work, Gaither *et al.* [19] revealed that unintended variations in the batch A etching process led to two different surface structures, namely, *regular* etch features, or scallops, which were expected with the Bosch DRIE process, and *irregular* etch features, denoted here as pits. The pits were likely formed when the SiO_2 isolation layer separating the device and handle layers was fractured during steps (b) or (c) in Fig. 1, leading to backside DRIE gases passing through the SiO_2 layer and re-etching the front-side surfaces during step (c) in Fig. 1. The formation of this unintended rough surface was not related to specimen geometry, affecting both the Durelli and arch designs roughly equally. The sidewall etch surfaces for the batches B and C samples are shown in Fig. 3(b) and (c), respectively [for reference, the images represent a portion of the web region, as indicated by the box in Fig. 3(a)]. In Fig. 3(b), the surface consists of regular etch scallops, which is similar to the batch A samples with the intended etch. However, Fig. 3(b) also revealed the following two important *differences* between batches A and B etch surfaces: 1) the scallop pitch increased from A to B due to an increase in both the passivation and etch step times and an ensuing decrease in the number of process loops required to etch through the entire Si device layer, and more notably and less obvious, 2) the overall etch quality improved from A to B due to the use of multiple (four) etch steps, which minimized scallop deterioration from wafer heating. In

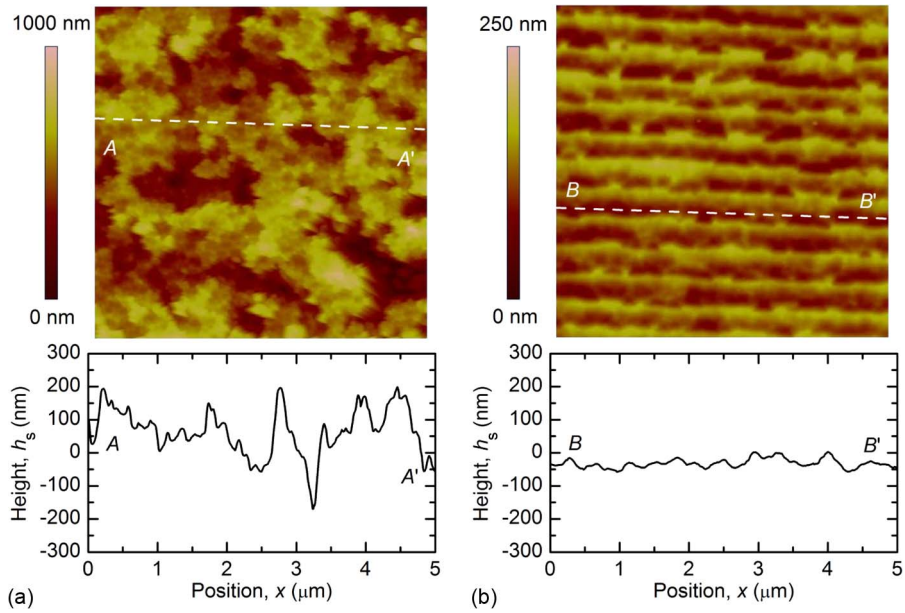

Fig. 4. (Top) AFM images with (bottom) corresponding line scans in the web loading direction of (a) batch A pitted surfaces and (b) batch A scallop surfaces. The line scans are on the same scale to highlight the difference in surface roughness.

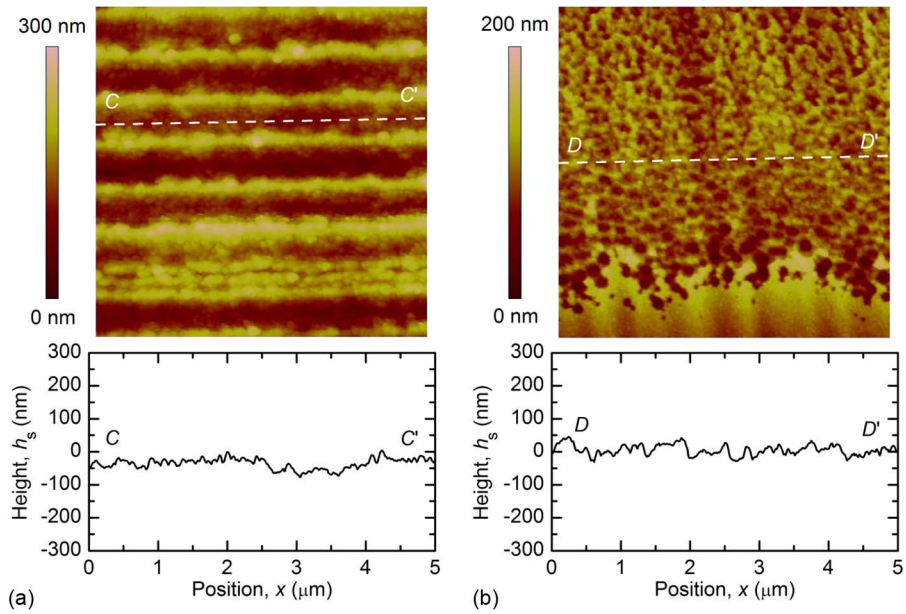

Fig. 5. (Top) AFM images with (bottom) corresponding line scans in the web loading direction of (a) batch B surfaces and (b) batch C surfaces. The line scans are on the same scale to highlight the difference in surface roughness.

Fig. 3(c), the etch process initially resulted in a smooth surface structure. In the latter stages of the etch process, however, the edges of the photoresist degraded, leading to unprotected front-side surfaces and, eventually, a heterogeneous sidewall surface structure. As is, the damage is localized to areas near the front side of the device layer, but if the etch was allowed to continue, the damage would eventually consume the entire surface, as with the batch A samples with the irregular etch.

Figs. 4 and 5 show AFM images and topographic line scans in the web loading direction for the batch A pitted [see Fig. 4(a)] and scallop surfaces [see Fig. 4(b)], the batch B surfaces [see Fig. 5(a)], and the batch C surfaces [see Fig. 5(b)]; the line scans are plotted on the same scale to highlight the vast differences in surface roughness. The results for h_{rms}, h_{pv}, and r_{scallop} are given in Table I. For the pitted samples, h_{rms} was 152.5 $\pm$ 14.6 nm, and h_{pv} for the individual surface features (not the maximum value over the line scan, as the peak and valley positions were irregular) in the loading direction was 197.6 $\pm$ 35.1 nm. Interestingly, the batches A and B scallops displayed significantly smaller values of h_{rms} with less variability, despite the large undulations of the scallops. Moreover, despite having different values for h_{rms} and r_{scallop}, the different scallops exhibited nearly identical values for h_{pv} parallel to the undulations and, most likely, perpendicular to a fracture-initiating flaw ($h_{\mathrm{pv}} \approx 35$ nm). The batch C samples showed the smallest RMS roughness; on average, h_{rms} was 20.3 nm. However, the large

TABLE I
SURFACE ROUGHNESS MEASUREMENTS, WHERE $h_{\rm rms}$ IS THE RMS HEIGHT VARIATION, $h_{\rm pv}$ IS THE PEAK-TO-VALLEY HEIGHT OF THE INDIVIDUAL SURFACE FEATURES, AND, FOR SAMPLES FABRICATED WITH THE BOSCH DRIE PROCESS, $r_{\rm scallop}$ IS THE SCALLOP PITCH. UNCERTAINTY VALUES REPRESENT ONE STANDARD DEVIATION FROM AT LEAST FOUR IMAGES[a] OR TWENTY LINE SCANS [b]

	Batch A Pitting Etch	*Batch A Small Scallops*	*Batch B Large Scallops*	*Batch C Cryo Etch*
$h_{\rm rms}$ (nm)[a]	152.5 ± 14.6	21.9 ± 0.2	48.0 ± 0.9	20.3 ± 4.7
$h_{\rm pv}$ (nm)[b]	197.6 ± 35.1	34.9 ± 2.4	34.8 ± 5.9	41.7 ± 18.8
$r_{\rm scallop}$ (nm)[b]	–	430.0 ± 6.5	666.2 ± 4.3	–

uncertainty in $h_{\rm rms}$ (4.7 nm) further proves that the surface structure is heterogeneous, as shown in Fig. 3(c). Consequently, the values for $h_{\rm pv}$ greatly vary, depending on the location across the web region. In more detail, $h_{\rm pv}$ was 65.5 ± 9.4 nm in the damaged region at the bottom of Fig. 3(c), 24.3 ± 4.0 nm in the smooth region in the middle of Fig. 3(c), and 35.5 ± 4.7 nm in the lightly pitted region at the top of Fig. 3(c). The latter two regions are also shown in Fig. 5(b). Overall, $h_{\rm pv}$ was found to be 41.7 ± 18.8 nm, as calculated from an equal number of measurements from each of the aforementioned three regions.

B. Mechanical Properties

Sample $P-h$ data were collected for each of the Durelli and arch theta test samples. Best fits to the linear sections of the responses generated compliance values that were all slightly greater than the values predicted from (3); the compliance differences for all samples ranged from 0.4 to 1.5 nm · mN^{-1}. For a typical peak load at sample failure of 1000 mN, this added compliance corresponds to about 0.4–1.5 μm of vertical displacement within the entire test system. This additional displacement is most likely due to shear deformation of the test strip surfaces relative to the mounting fixture, and assuming the deformation occurs uniformly over the entire height (1.03 mm) of the test strip translates to approximately 0.1% shear strain at the interface. The test system compliance values reported here are different than previously reported results [19]. The variability in compliance is due to subtle differences in the test strip mounting process and was thus removed from the data with a sample-specific compliance correction. Fig. 6 shows a compliance-corrected $P-h$ trace for a sample tested to failure. In this particular experiment, the test sample was loaded to 400 mN and unloaded to 200 mN several times, before finally being loaded to failure. The initial nonlinear region at small P was probably due to the contacting and seating of the sapphire indenter sphere on the rough etched surface of the specimen. After the initial seating process, the $P-h$ traces for all the loading cycles between 200 and 400 mN were indistinguishable and linear, which is indicative of a negligible subsequent hysteresis and a completely elastic response. P and h were also converted into σ and ε using (1) and (2). The strength of this sample, as determined from the stress at peak load, was found to be 2.72 GPa, which was consistent with other results for micromachined single-crystal silicon with similar stressed areas [19].

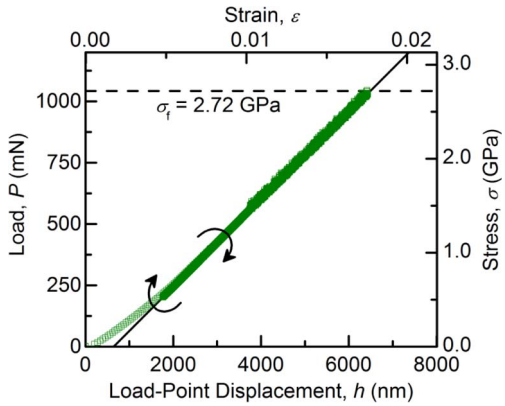

Fig. 6. Load-displacement and corresponding stress–strain data for a test sample loaded to failure. The sample was loaded to a peak load of 400 mN, cycled between 200 and 400 mN twice, and subsequently loaded to failure. After the nonlinear portion of the initial loading segment, the $P-h$ trace remained linear, as demonstrated by the solid line, throughout the cyclic loading and sample failure measurements. The strength of the sample, determined at maximum P, was 2.72 GPa.

The resulting strength σ_f values for all of the Durelli and arch theta samples are plotted as a function of sample web width in Fig. 7. For batch A, samples with the intended etch and near-ideal web widths, henceforth referred to as the small scallop samples, had greater strengths than samples with the unintended etch and reduced web widths, henceforth referred to as the pitting etch samples. The average values for w and σ_f were 7.8 μm and 2.1 GPa, respectively, for the small scallop samples and 5.6 μm and 1.2 GPa, respectively, for the pitting etch samples. In addition, samples with small scallops exhibited less variability across a given web region, as evident by the decrease in the average web width uncertainty in Fig. 7(a), where the horizontal bars represent one standard deviation. The change in variability was evident when capturing images for the web width calculation routine; samples with smaller web widths had rougher sample edges, most notably in the web region. The batch B, or large scallop, samples and batch C, or cryo etch, samples also exhibited small variability in the individual web regions, as demonstrated in Fig. 7(a) and, more readily, in Fig. 7(b). The slight decrease in the average web width for both sample sets is most likely due to overexposure during the front-side photolithography, as shown in Fig. 1(b). Despite the decrease in average web width, the samples exhibited similar fracture strengths; the average value for σ_f was 2.1 GPa for the large scallop samples and 2.4 GPa for the cryo etch samples.

Fig. 8 is a plot of the cumulative failure probability P_f as a function of strength σ_f for all sample sets. Gaither *et al.* [19] noted that the entire strength distribution of the batch A samples was bimodal, primarily due to the formation of two different flaw populations (pitting flaws and small scallops), with a strength range of approximately 1.4–1.9 GPa separating the low and high strength distributions. Using this demarcation, the strength values for the two strength distributions ranged from 0.8 to 1.9 GPa and 1.4 to 2.7 GPa. Moreover, the strength distribution for the large scallop samples (1.6–2.5 GPa) was similar to that of the small scallop samples, whereas the distribution for the cryo etch samples (1.4–3.1 GPa) was greater

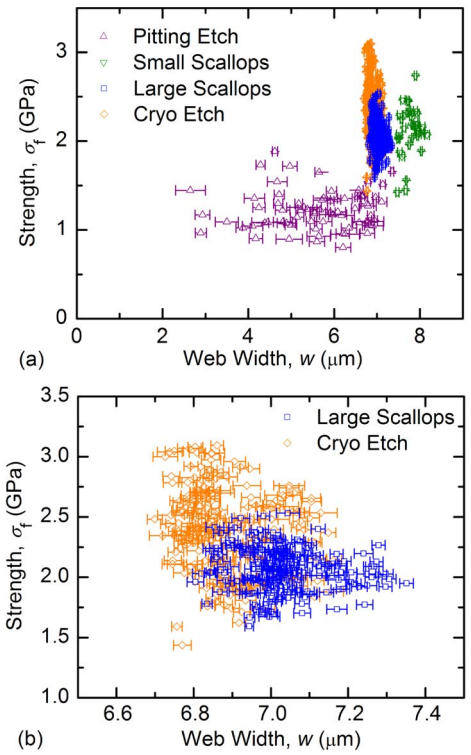

Fig. 7. Fracture strength as a function of web width for (a) all samples and (b) batches B and C samples. In general, the samples with the intended surface structures exhibited less variability from sample to sample and across a given web section.

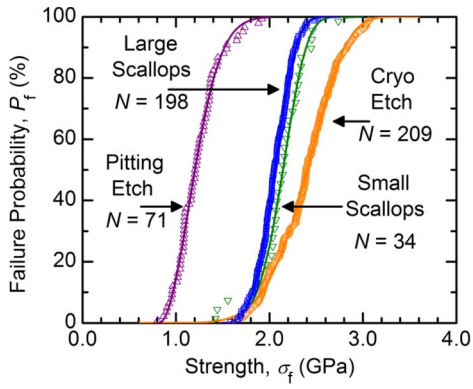

Fig. 8. Strength distributions and corresponding three-parameter Weibull failure probability plots for each of the four sample sets. The strength distribution for the batch A samples was bimodal, primarily due to the formation of two different flaw populations, and the resulting distribution for the samples with the small scallops was similar to that for samples with large scallops. Additionally, the cryogenic etch resulted in larger strength values on average, but with a larger distribution.

on average, but with a larger spread in the overall distribution. Using these strength ranges with (12) results in c_s ranges of 200–35 nm for the pitting etch, 65–18 nm for the small scallops, 50–20 nm for the large scallops, and 65–13 nm for the cryo etch. Setting $a = h_{\rm pv}$ and using the estimated values for c_s in (13) suggest c_f values in the range of a few nanometers to a few tens of nanometers. Miller *et al.* [28] reported nearly identical σ_f and c_s ranges for Bosch DRIE-etched single-crystal silicon, but with a completely different pull-tab tensile specimen. Of the three sample sets fabricated, two were found to possess the intended scallop features, giving rise to fracture strengths (1.4–2.5 GPa) in good agreement with results from the small and large scallop samples. In contrast, the third set displayed extensive sidewall damage, yielding fracture strengths (1.0–1.8 GPa) similar to those observed with the pitting etch samples.

IV. Discussion

A key feature of the theta specimen fabrication and testing methodology is that the strengths of a large number of samples can be measured, such that the strength distribution resulting from a given processing sequence can be determined with great precision. If the same processing sequence is used in the fabrication of components of MEMS devices, then the strength distribution of the components is known with similar precision and can be used by MEMS designers to optimize component mechanical reliability—the ability of a component to support a required load over a specified lifetime. In designing for component reliability, knowledge of the variation of load applied to the component with time t is required, and, in particular, the variation with time of the maximum load and, thus, the maximum stress experienced by the component. A comparison of this maximum experienced stress $\sigma_{\max}$ with the threshold strength $\sigma_{\rm th}$ of the component strength distribution leads to a choice in designing for reliability that depends on the flexibility in selecting the geometry of the MEMS component. If the geometry of the MEMS component can be selected such that the maximum load leads to the maximum experienced stress never exceeding the threshold strength, that is, $\sigma_{\max} < \sigma_{\rm th}$ over the desired lifetime of the component, then the component will never fail, and the reliability is then deterministic. The simplest example is for a component in tension, as here, in which the component cross-sectional area can be made large enough such that $\sigma_{\max}$ is sufficiently less than $\sigma_{\rm th}$ with a margin of safety. If, however, the geometry of the MEMS component cannot be selected to meet this condition, then there is a likelihood that some components will fail prior to the desired lifetime, and the reliability is then probabilistic. In the first (deterministic) case, the details of the variation in applied stress with time and the details of the component strength distribution do not matter. In this case, MEMS design attention focuses on the processing–structure–property relations associated with setting the required $\sigma_{\rm th}$. In the second (probabilistic) case, the variation of the maximum stress with time $\sigma_{\max}(t)$ is convoluted with the cumulative failure probability $P_f(\sigma_f)$ to generate the component reliability $R(t) = 1 - P_f(t)$, where $P_f(t)$ is the cumulative probability of component failure as a function of time, and $R(t)$ is the proportion of remaining intact components. In this case, MEMS design attention focuses on the property–performance linkages associated with predicting $P_f(t)$ and the full set of parameters describing the strength distribution, m, σ_θ, and $\sigma_{\rm th}$, along with the specific form of $\sigma_{\max}(t)$. The discussion here will focus on the processing–structure–property relationships and property–performance predictions for the theta specimen in turn.

TABLE II
THREE-PARAMETER WEIBULL DISTRIBUTION FITS FOR THE STRENGTH DATA, WHERE N IS THE NUMBER OF SAMPLES, m IS THE WEIBULL MODULUS, σ_θ IS THE SCALING STRENGTH, AND $\sigma_{\rm th}$ IS THE THRESHOLD STRENGTH. UNCERTAINTY VALUES REPRESENT A 68% CONFIDENCE LEVEL IN THE FIT

	Batch A Pitting Etch	*Batch A Small Scallops*	*Batch B Large Scallops*	*Batch C Cryo Etch*
N	71	34	198	209
m	2.00 ± 0.12	4.57 ± 1.18	3.73 ± 0.12	5.73 ± 0.27
σ_θ (GPa)	0.46 ± 0.02	0.90 ± 0.26	0.66 ± 0.02	1.84 ± 0.09
$\sigma_{\rm th}$ (GPa)	0.82 ± 0.02	1.32 ± 0.24	1.46 ± 0.02	0.67 ± 0.09

A. Processing–Structure–Property Relationships

The measurements on the etched Si samples demonstrated that the theta specimen can be utilized to achieve a materials science and engineering objective of forming *processing–structure–property* relationships. Variations in the etching process led to several different surface structures (see Figs. 3–5) that, in turn, led to several different strength properties (Figs. 7 and 8). To obtain quantitative insight into the relationships, the strength data from each distribution were fit to a three-parameter Weibull distribution function, as described by (10). The solid lines in Fig. 8 represent the best fit distributions, which are described by the m, σ_θ, and $\sigma_{\rm th}$ values in Table II. Of particular interest here is $\sigma_{\rm th}$, as it denotes the stress below which a specimen will not fail and, thus, represents a valuable metric for enhancing MEMS yield and reliability. In general, $\sigma_{\rm th}$ varied by about a factor of 2, indicating that fracture strength was influenced by surface structure. On closer inspection, it is clear that the $\sigma_{\rm th}$ values for samples with the small and large scallops were: 1) within experimental uncertainty and 2) about a factor of 2 greater than the $\sigma_{\rm th}$ values for samples with the pitting and cryo etch.

In reference to point 1), the samples formed from intended etch processes (i.e., small and large scalloped samples) exhibited almost identical $h_{\rm pv}$, and thus a, values, as shown in Table I. In addition, the σ_f distributions for the two scallop sample sets were virtually the same, which pointed to a nearly identical c_s distribution using (12). From (13), the c_f distributions were therefore the same, indicating that the strength may not depend on the scallop height or pitch but on subsurface flaws generated by, and inherent to, the Bosch DRIE process. In reference to point 2), the samples with diminished $\sigma_{\rm th}$ (i.e., pitted and cryo etch samples) exhibited large $h_{\rm pv}$ or large variability in $h_{\rm pv}$ or both, as shown in Table I. For instance, the pitted samples exhibited both large $h_{\rm pv}$ and large variability in $h_{\rm pv}$; the extent of cracking in the SiO_2 isolation layer differed across the wafer, not only allowing the backside DRIE gases to roughen the front-side surfaces but also to roughen the surfaces in varying amounts. Therefore, both the average value and the uncertainty for c_s increased, as given by (13). The increase in the average *value* of c_s decreased the characteristic strength, whereas the increase in the *uncertainty* for c_s increased the fracture strength variability, both of which led to a smaller $\sigma_{\rm th}$. In contrast, the cryo samples possessed only large variability in $h_{\rm pv}$; the average values were similar to those for the scalloped samples. Here, the heterogeneous surface structure was due to edge degradation of the photoresist on the front-side surfaces in the latter stages of the etching process and, thus, transpired over all of the samples uniformly. Because of the heterogeneous surface structure and the multiple flaw types that likely ensue, the strength data are ill defined by a single Weibull distribution function [11] and will therefore predict an unreasonable value for $\sigma_{\rm th}$. There are two symptoms that point to this occurring with the cryo etch strength distribution. First, there is a significant change in the shape of the σ_f distribution around 2.3 GPa, which could suggest the presence of a second low-strength flaw population. Second, the difference between the smallest experimental σ_f and $\sigma_{\rm th}$ is $\approx$0.7 GPa for the cryo etch samples but < 0.2 GPa for the other three surface structures, indicating that the Weibull distribution function may not accurately represent the data. Interestingly, if the cryo strength distribution is split at $\approx$2.3 GPa, the upper distribution has a $\sigma_{\rm th}$ of 2.2 GPa and the lower distribution has a $\sigma_{\rm th}$ of 1.2 GPa, both of which are within 0.2 GPa of the smallest σ_f.

Because of the difficulties associated with specimen gripping, loading alignment, and posttest sample collection and manipulation at small scales, previous studies on the fracture strength of single-crystal silicon have been limited to small data sets (tens of samples), hindering the ability to accurately describe the lower tail of the distribution [9]–[11], [18], [28]–[35]. As a result, most of the studies resort to the two-parameter simplification of the Weibull distribution function, which underestimates the strength values in the tail and, consequently, provides a conservative distribution, by assuming $\sigma_{\rm th}$ is zero. Recently, high-throughput techniques have enabled larger data sets (hundreds and, often, thousands of samples) and the ability to determine $\sigma_{\rm th}$ through a fit to the three-parameter Weibull distribution function. As an example, Boyce [13] used a slack-chain concept to test thousands of specimens at a rate of one per minute. The polycrystalline silicon (polysilicon) test specimens were fabricated from the Sandia Ultra-planar Multi-level MEMS Technology process flow and tested using a custom probe station that mitigated the effects of substrate friction. The three-parameter fit to the data resulted in $m = 7.7$, $\sigma_\theta = 1.2$ GPa, and $\sigma_{\rm th} = 1.4$ GPa. Reedy *et al.* [36] later compared additional slack-chain data with results from an on-chip method [14]; three-parameter Weibull fits to the slack-chain and on-chip data resulted in $m = 5.8$, $\sigma_\theta = 1.0$ GPa, and $\sigma_{\rm th} = 1.8$ GPa; and $m = 3.0$, $\sigma_\theta = 0.5$ GPa, and $\sigma_{\rm th} = 2.1$ GPa, respectively. On the surface, it appears as if the aforementioned characteristic strengths ($\sigma_c = \sigma_\theta + \sigma_{\rm th}$) for polysilicon are greater than those in this study for single-crystal silicon. However, prior to comparing the results, it is necessary to account for the markedly different stressed areas A_s. As shown in the Appendix, σ_θ scales with A_s according to

$$\sigma_{\theta 2}/\sigma_{\theta 1} = (A_{s1}/A_{s2})^{1/m} \tag{14}$$

where $\sigma_{\theta 1}$ and A_{s1} are the original scaling strength and stressed area, respectively; and $\sigma_{\theta 2}$ and A_{s2} are the scaled scaling strength and stressed area, respectively (m and $\sigma_{\rm th}$ remain constant throughout the scaling process). From fractography on both the single-crystal silicon samples and the polysilicon samples, it is clear that fractures initiate only along the

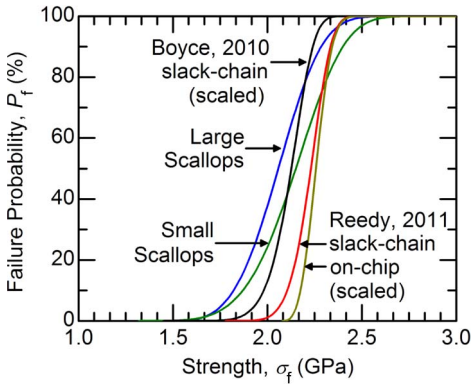

Fig. 9. Scaled three-parameter Weibull failure probability plots for the small scallop data, large scallop data, first slack-chain data [13], second slack-chain data [36], and on-chip data [36]. σ_c values for the various distributions are within 0.2 GPa of each other.

sidewalls. For the single-crystal silicon samples, fracture initiated on a {110} plane at an etch-induced surface feature and, after a small propagation distance, deflected onto the smaller fracture energy {111} planes [18], [19]. For the polysilicon samples, fracture initiated at a grain boundary and propagated according to the polysilicon crystallography [12], [13], [36]. As a result, the stressed area was taken as the surface area of the two sidewalls, resulting in $A_{s1} = 93.2\ \mu\text{m}^2$ for the slack-chain geometry, $A_{s1} = 326.2\ \mu\text{m}^2$ for the on-chip geometry, and $A_{s2} = 6250\ \mu\text{m}^2$ for the theta geometry. Using (14) (and σ_θ referenced earlier as $\sigma_{\theta 1}$ for each data set), $\sigma_{\theta 2} = 0.7$ GPa for the first slack-chain data [13], $\sigma_{\theta 2} = 0.5$ GPa for the second (additional) slack-chain data [36], and $\sigma_{\theta 2} = 0.2$ GPa for the on-chip data [36]. As displayed in Fig. 9, each of these values can be used in conjunction with the corresponding m and σ_{th} to create scaled versions of the original distributions, which then exemplify some of the same characteristics as the distributions for the scalloped surfaces. For example, the σ_c values for the various distributions are within 0.2 GPa of each other. It is important to note that this does not imply that the *flaw sizes* are comparable, as T and Ψ are different for single-crystal silicon and polysilicon. In fact, the only conclusion that can be drawn from this observation is that the *flaw potency* $\Psi c_s^{1/2}$ is about 1.5 times larger in polysilicon than in single-crystal silicon, given that T is 1.1 MPa $\cdot$ m$^{1/2}$ for the former [37], [38] and 0.71 MPa $\cdot$ m$^{1/2}$ for the (110) plane of the latter [25].

B. Property–Performance Predictions

An additional technologically important goal of materials science and engineering is to establish the linkage between material *properties* and the *performance* of components formed from that material. The theta specimen can be used to great effect to predict the manufacturing yield and operational reliability of MEMS components if the spectrum of the time maximum stress $\sigma_{\max}(t)$ is known throughout the manufacturing or operational period. Two approaches to predicting reliability when the condition $\sigma_{\max} > \sigma_{\text{th}}$ is met during this period will be demonstrated here, using the strength distribution of theta specimens formed with large scallops as an illustration.

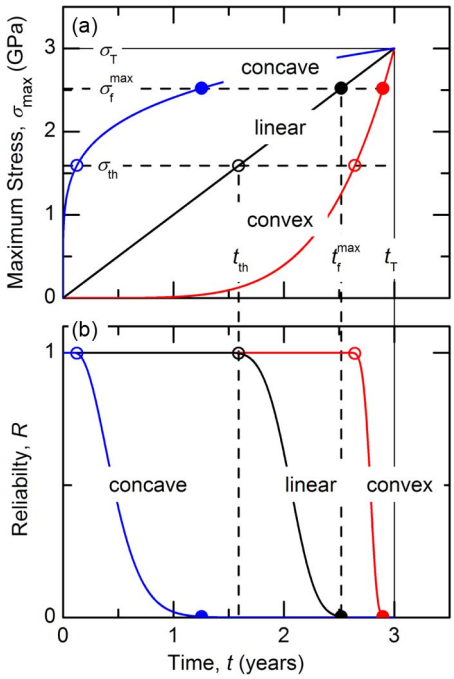

Fig. 10. Reliability prediction simulations for different applied stress functions as a function of time. (a) Concave, linear, and convex relationships for applied stress as a function of time, assuming an applied stress of 0–3 GPa over a time of three years. The open and closed circles indicate the time at which the applied stress reaches the threshold strength and the maximum failure stress, respectively. (b) Reliability curves as a function of time for each of the three applied stress curves in (a).

In the first approach to reliability prediction, the spectrum $\sigma_{\max}(t)$ will be explicitly assumed with a simple power-law form, i.e.,

$$\sigma_{\max}(t) = \sigma_T (t/t_T)^n. \tag{15}$$

$\sigma_{\max}$ increases from zero at the start of the time period $t = 0$ to a maximum value σ_T at the end of the time period $t = t_T$ with a dependence determined by the exponent n. The values assumed here are $\sigma_T = 3$ GPa; $t_T = 3$ years; and $n = 0.2$, 1, and 5 for concave, linear, and convex variations of $\sigma_{\max}$ with t, respectively. Generating the reliability prediction is then a simple matter of replacing σ_f with $\sigma_{\max}(t)$ in (10) and combining (10) and (15) as a parametric set to generate $P_f(t)$. Fig. 10 is a plot of reliability predictions for components containing the large scallop surface finish using the aforementioned stress variation parameters and the strength distribution parameters from Table II. Fig. 10(a) shows $\sigma_{\max}(t)$, and Fig. 10(b) shows $R(t)$. Consider first the linear $(n = 1)$ variation of $\sigma_{\max}(t)$: $\sigma_{\max}$ linearly increases from zero until, at time $t = t_{\text{th}}$, the condition $\sigma_{\max} = \sigma_{\text{th}}$ is reached, which is indicated by the open symbols on the plots. Prior to this time, no components fail, which is indicated by a reliability of 1. At time $t = t_f^{\max}$, the condition $\sigma_{\max} = \sigma_f^{max}$ is reached, which is indicated by the solid symbols on the plots, where $\sigma_f^{\max}$ is the maximum failure strength in the strength distribution. Time $t_f^{\max}$ is the lifetime of the longest surviving component, and by this time, all components have failed, as indicated by a reliability of 0. For intermediate times, $t_{\text{th}} < t < t_f^{\max}$, the reliability decreases from 1 to 0, and this decrease is seen to be the mirror image

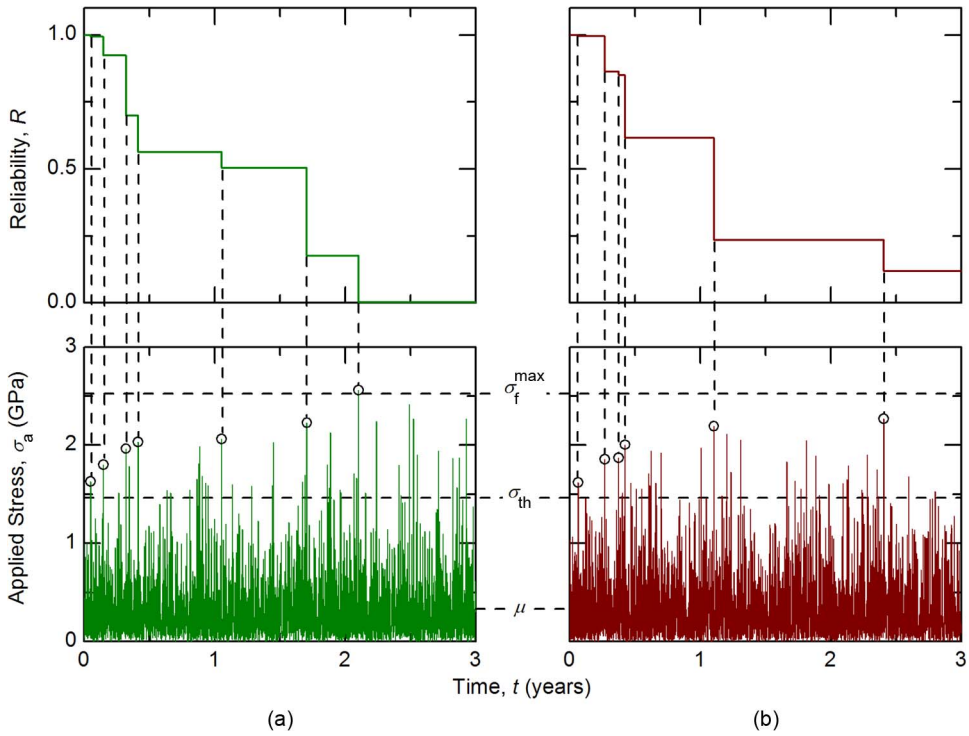

Fig. 11. Reliability prediction simulations for a randomly applied stress as a function of time. In (a), all components are destroyed over a time of three years, whereas in (b), some components remain intact over a time of three years.

of the strength distribution in Fig. 8. For the convex $(n = 5)$ variation of $\sigma_{\max}(t)$, the initial period for which no components fail is greater than for the linear variation because the time is greater for the condition $\sigma_{\max} = \sigma_{\rm th}$ to be reached, which is again indicated by the open symbols. However, the increase in $\sigma_{\max}$ with t from this condition is more rapid than for the linear case such that the decrease in reliability takes place more rapidly, until all of the components have failed, which is again indicated by the solid symbols. The concave $(n = 0.2)$ variation of $\sigma_{\max}(t)$ displays the opposite variation from linear than the convex: The initial period for which no components fail is very short, and the subsequent decrease in reliability takes place more slowly. In all cases, the reliability variation with time is seen to include an initial period with no failures, until the maximum stress experienced reaches the threshold strength, which is followed by a decrease in reliability that is a variably deformed mirror image of the strength distribution; in the cases here, the maximum applied stress was taken to be greater than the maximum failure strength, leading to a final stage in which all components had failed.

In the second approach to reliability prediction, the variation of $\sigma_{\max}(t)$ is assumed to be stochastic, with the values for applied stress σ_a obeying an assumed exponential probability density distribution, i.e.,

$$P_a(\sigma_a) = (1/\mu)\exp(-\sigma_a/\mu) \tag{16}$$

where μ is the mean of the distribution. Values of σ_a were randomly sampled from this distribution, representing the stress applied to a component in sequential discrete time steps, which is here assumed to represent 0.001 year. Three thousand values were sampled, representing three years of exposure to stress, and the value of $\mu = 0.329$ GPa was used, corresponding to the likelihood of a single stress value of $\sigma_a = 3$ GPa randomly occurring in the three-year period. Two example simulations are shown in Fig. 11. To generate the reliability predictions, the value of σ_a at time t was compared with the current component strength distribution, and all remaining components with strengths less than σ_a were regarded as having failed at that time. The bottom graphs in Fig. 11(a) and (b) show the simulated applied stress spectrums as a function of time. Most stress values occurred near the mean, but occasionally, a significantly larger value occurred. The largest stress value to have occurred at a given time t is $\sigma_{\max}(t)$, and those greater than $\sigma_{\rm th}$ are indicated in the graphs by open symbols. Note that $\sigma_{\max}(t)$ increases with time, just as in the explicit formulation shown in Fig. 10, but in a stochastic manner. The top graphs in Fig. 11(a) and (b) show reliability as a function of time for the two simulated stress spectra. As in the explicit formulation, there is a time delay before the first components fail, and the reliability is reduced. As time proceeds, the reliability remains fixed at discrete values as the simulated values of the applied stress do not increase $\sigma_{\max}$, that is, $\sigma_a(t) < \sigma_{\max}(t)$; when the condition $\sigma_a(t) > \sigma_{\max}(t)$ is met, large groups of the remaining weakest components fail and the reliability decreases in discrete steps. If the simulated stress meets the condition $\sigma_{\max} > \sigma_f^{\max}$, all components have failed, as shown in the reliability plot in Fig. 11(a); if this condition does not occur in the probabilistic stress spectrum, then some components will remain intact at the end of the simulation, as shown in the reliability plot in Fig. 11(b). Note that simulations such as this will nearly always lead to effectively concave variations of $\sigma_{\max}(t)$ and will lead to stretched versions of the mirror image of the strength distribution for $R(t)$. This effect will be

compounded if the strength distribution $P_f(\sigma_f)$ is very broad, for example, for that of the cryogenic etch, rather than the large scallop etch assumed here (see Fig. 8). In the case of a broad strength distribution, the reliability behavior will tend to that in Fig. 11(b) rather than that in Fig. 11(a).

V. Summary and Conclusion

In summary, the theta test specimen has been used to examine etching process effects on surface structure, fracture strength, and reliability of single-crystal silicon. Three different batches of theta specimens were fabricated, two with DRIE and one with temperature-controlled cryogenic plasma etching. Variations in the etching process led to different surface structures, which, in turn, led to different strength properties. In general, the threshold strength varied by approximately a factor of 2, indicating that fracture strength was related to surface structure. On closer inspection, it is clear that the threshold strength for samples with the small and large scallops were: 1) within experimental uncertainty and 2) approximately a factor of 2 greater than the values for samples with the pitting and cryo etch. In reference to point 1), the scalloped samples exhibited nearly identical crack length distributions, indicating that the strength may not depend on the scallop height or pitch but on subsurface flaws generated by, and inherent to, the Bosch DRIE process. In reference to 2), the pitted and cryo etch samples exhibited large variability in their peak-to-valley heights; in both cases, the variability was due to a heterogeneous surface structure generated during an unintentional etch of the Si device layer. The characteristic strengths for the scalloped surfaces were found to be similar to those for polysilicon, after the latter strength distributions were scaled to account for differences in the stressed area. It is important to note, however, that this does not imply that the flaw sizes were comparable, but only that the flaw potency in polysilicon is greater than in single-crystal silicon. Finally, to demonstrate how the strength data can be utilized to predict reliability, one of the strength distributions was used in conjunction with both explicit and stochastic loading schemes to assess the effect of the loading schemes on the lifetime spectrum of a device.

Appendix
Scaling Relationship for σ_θ and A_s

The three-parameter Weibull probability distribution used to describe the strengths of theta and other test specimens, i.e., (10), includes no information with regard to specimen dimensions. Weakest link concepts indicate that specimens with strengths controlled by surface flaws should exhibit different strength distributions as the specimen stressed surface area is altered. In particular, larger specimens should exhibit weaker strengths, as the probability of including larger flaws is increased. Area scaling analyses for specimen strengths described by the three-parameter Weibull distribution are not prevalent in the literature, and here, such an analysis is outlined. The two key elements to such an analysis are that a flaw distribution exists on the surface of specimens that is independent of specimen size and that the specimen failure probability distribution requires summing over all the "links" comprising the specimen surface. In practice, specimen size-independent strengths determined by the flaw distribution are used, and the sum is converted to an integral, giving

$$P_f = 1 - \exp\left\{-\lambda \int_{A_s} \left[(\sigma_f - \sigma_{\rm th})/\sigma_0\right]^m dS\right\} \tag{A1}$$

where λ is the number density of strength-controlling flaws per area [39]; A_s is the stressed area; and m, σ_0, and $\sigma_{\rm th}$ are the Weibull parameters that describe the size-invariant distribution. Under simple tension, this becomes

$$P_f = 1 - \exp\left\{-(\lambda A_s)\left[(\sigma_f - \sigma_{\rm th})/\sigma_0\right]^m\right\} \tag{A2}$$

and it is apparent that strengths do decrease as specimen area A_s increases. A comparison of this equation with (10) shows that the parameter σ_θ that describes a measured strength distribution of specimens of a specific size is related to the size-invariant parameter σ_0 by

$$(\lambda A_s)\,(1/\sigma_0^m) = (1/\sigma_\theta^m)\,. \tag{A3}$$

In particular, for two sets of specimens of stressed areas A_{s1} and A_{s2}, parameter σ_θ scales as

$$\sigma_{\theta 2}/\sigma_{\theta 1} = (A_{s1}/A_{s2})^{1/m}. \tag{A4}$$

The threshold strength and the Weibull modulus are not affected by the change in specimen area, $\sigma_{\rm th2} = \sigma_{\rm th1}$, and $m_2 = m_1$.

Acknowledgment

The authors would like to thank G. D. Quinn of the National Institute of Standards and Technology (NIST) for guidance with Weibull statistics. Research was performed in part at the NIST Center for Nanoscale Science and Technology. Certain commercial equipment, instruments, or materials are identified in this paper in order to specify the experimental procedure adequately. Such identification is not intended to imply recommendation or endorsement by NIST nor is it intended to imply that the materials or equipment identified are necessarily the best available for the purpose.

References

[1] G. T. A. Kovacs, *Micromachined Transducers Sourcebook*. New York: McGraw-Hill, 1998.
[2] F. W. DelRio, M. P. de Boer, J. A. Knapp, E. D. Reedy, P. J. Clews, and M. L. Dunn, "The role of van der Waals forces in adhesion of micromachined surfaces," *Nat. Mater.*, vol. 4, no. 8, pp. 629–634, 2005.
[3] F. W. DelRio, M. L. Dunn, and M. P. de Boer, "Capillary adhesion model for contacting micromachined surfaces," *Scripta Mater.*, vol. 59, no. 9, pp. 916–920, Nov. 2008.
[4] A. D. Corwin and M. P. deBoer, "Effect of adhesion on dynamic and static friction in surface micromachining," *Appl. Phys. Lett.*, vol. 84, no. 13, pp. 2451–2453, Mar. 2004.
[5] A. D. Corwin and M. P. de Boer, "Frictional aging, de-aging and re-aging in a micromachined interface," *Phys. Rev. B*, vol. 81, no. 17, pp. 174109-1–174109-11, May 2010.
[6] B. G. Bush, F. W. DelRio, C. Jaye, D. A. Fischer, and R. F. Cook, "Interfacial mechanical properties of n-alkylsilane monolayers on silicon substrates," *J. Microelectromech. Syst.*, to be published.

[7] J. D. Lord, B. Roebuck, R. Morrell, and T. Lube, "Aspects of strain and strength measurement in miniaturized testing for engineering metals and ceramics," *Mater. Sci. Technol.*, vol. 26, no. 2, pp. 127–148, 2010.
[8] W. N. Sharpe, B. Yuan, and R. L. Edwards, "A new technique for measuring the mechanical properties of thin films," *J. Microelectromech. Syst.*, vol. 6, no. 3, pp. 193–199, Sep. 1997.
[9] F. Ericson and J. A. Schweitz, "Micromechanical fracture strength of silicon," *J. Appl. Phys.*, vol. 68, no. 11, pp. 5840–5844, Dec. 1990.
[10] T. Namazu, Y. Isono, and T. Tanaka, "Evaluation of size effect on mechanical properties of single crystal silicon by nanoscale bending test using AFM," *J. Microelectromech. Syst.*, vol. 9, no. 4, pp. 450–459, Dec. 2000.
[11] K. S. Chen, A. Ayon, and S. M. Spearing, "Controlling and testing the fracture strength of silicon on the mesoscale," *J. Amer. Ceram. Soc.*, vol. 83, no. 6, pp. 1476–1484, Jun. 2000.
[12] B. L. Boyce, J. M. Grazier, T. E. Buchheit, and M. J. Shaw, "Strength distributions in polycrystalline silicon MEMS," *J. Microelectromech. Syst.*, vol. 16, no. 2, pp. 179–190, Apr. 2007.
[13] B. Boyce, "A sequential tensile method for rapid characterization of extreme-value behavior in microfabricated materials," *Exp. Mech.*, vol. 50, no. 7, pp. 993–997, Sep. 2010.
[14] S. S. Hazra, M. S. Baker, J. L. Beuth, and M. P. de Boer, "Demonstration of an in situ on-chip tensile tester," *J. Micromech. Microeng.*, vol. 19, no. 8, pp. 082001-1–082001-5, Aug. 2009.
[15] G. D. Quinn, E. Fuller, D. Xiang, A. Jillavenkatesa, L. Ma, D. Smith, and J. Beall, "A novel test method for measuring mechanical properties at the small-scale: The theta specimen," *Ceram. Eng. Sci. Proc.*, vol. 26, no. 2, pp. 117–126, 2005.
[16] E. R. Fuller, D. L. Henann, and L. Ma, "Theta-like specimens for measuring mechanical properties at the small-scale: Effects of non-ideal loading," *Int. J. Mater. Res.*, vol. 98, no. 8, pp. 729–734, 2007.
[17] A. J. Durelli, S. Morse, and V. Parks, "The theta specimen for determining tensile strength of brittle materials," *Mater. Res. Std.*, vol. 2, no. 2, pp. 114–117, 1962.
[18] M. S. Gaither, F. W. DelRio, R. S. Gates, E. R. Fuller, and R. F. Cook, "Strength distribution of single-crystal silicon theta-like specimens," *Scripta Mater.*, vol. 63, no. 4, pp. 422–425, 2010.
[19] M. S. Gaither, F. W. DelRio, R. S. Gates, and R. F. Cook, "Deformation and fracture of single-crystal silicon theta-like specimens," *J. Mater. Res.*, vol. 26, no. 20, pp. 2575–2589, Oct. 2011.
[20] W. Kern and D. A. Puotinen, "Cleaning solution based on hydrogen peroxide for use in semiconductor technology," *RCA Rev.*, vol. 31, pp. 187–206, Jun. 1970.
[21] S. D. Senturia, *Microsystem Design*. Boston, MA: Kluwer, 2001.
[22] S. Tachi, K. Tsujimoto, and S. Okudaira, "Low-temperature reactive ion etching and microwave plasma-etching of silicon," *Appl. Phys. Lett.*, vol. 52, no. 8, pp. 616–618, Feb. 1988.
[23] H. J. McSkimin and P. Andreatch, "Measurement of third-order moduli of silicon and germanium," *J. Appl. Phys.*, vol. 35, no. 11, pp. 3312–3319, Nov. 1964.
[24] B. Holm, R. Ahuja, Y. Yourdshahyan, B. Johansson, and B. I. Lundqvist, "Elastic and optical properties of σ- and κ-Al_2O_3," *Phys. Rev. B*, vol. 59, no. 20, pp. 12 777–12 787, May 1999.
[25] R. F. Cook, "Strength and sharp contact fracture of silicon," *J. Mater. Sci.*, vol. 41, no. 3, pp. 841–872, Feb. 2006.
[26] B. R. Lawn, *Fracture of Brittle Solids*. Cambridge, U.K.: Cambridge Univ. Press, 1993.
[27] Y. Yamamoto, Y. Sumi, and K. Ao, "Stress intensity factors of cracks emanating from semi-elliptical side notches in plates," *Int. J. Fracture*, vol. 10, no. 4, pp. 593–595, Dec. 1974.
[28] D. C. Miller, B. L. Boyce, M. T. Dugger, T. E. Buchheit, and K. Gall, "Characteristics of a commercially available silicon-on-insulator MEMS material," *Sens. Actuators A, Phys.*, vol. 138, no. 1, pp. 130–144, Jul. 2007.
[29] J. Vedde and P. Gravesen, "The fracture strength of nitrogen doped silicon wafers," *Mater. Sci. Eng. B*, vol. 36, no. 1–3, pp. 246–250, Jan. 1996.
[30] J.-Å. Schweitz and F. Ericson, "Evaluation of mechanical materials properties by means of surface micromachined structures," *Sens. Actuators A, Phys.*, vol. 74, no. 1–3, pp. 126–133, Apr. 1999.
[31] K. S. Chen, A. A. Ayon, X. Zhang, and S. M. Spearing, "Effect of process parameters on the surface morphology and mechanical performance of silicon structures after deep reactive ion etching (DRIE)," *J. Microelectromech. Syst.*, vol. 11, no. 3, pp. 264–275, Jun. 2002.
[32] S. Sundararajan, B. Bhushan, T. Namazu, and Y. Isono, "Mechanical property measurements of nanoscale structures using an atomic force microscope," *Ultramicroscopy*, vol. 91, no. 1–4, pp. 111–118, May 2002.
[33] T. Tsuchiya, M. Hirata, N. Chiba, R. Udo, Y. Yoshitomi, T. Ando, K. Sato, K. Takashima, Y. Higo, Y. Saotome, H. Ogawa, and K. Ozaki, "Cross comparison of thin-film tensile-testing methods examined using single-crystal silicon, polysilicon, nickel, and titanium films," *J. Microelectromech. Syst.*, vol. 14, no. 5, pp. 1178–1186, Oct. 2005.
[34] T. Alan, A. T. Zehnder, D. Sengupta, and M. A. Hines, "Methyl monolayers improve the fracture strength and durability of silicon nanobeams," *Appl. Phys. Lett.*, vol. 89, no. 23, pp. 231905-1–231905-3, Dec. 2006.
[35] L. Banks-Sills, J. Shklovsky, S. Krylov, H. A. Bruck, V. Fourman, R. Eliasi, and D. Ashkenazi, "A methodology for accurately measuring mechanical properties on the micro-scale," *Strain*, vol. 47, no. 3, pp. 288–300, Jun. 2011.
[36] E. D. Reedy, B. L. Boyce, J. W. Foulk, R. V. Field, M. P. de Boer, and S. S. Hazra, "Predicting fracture in micrometer-scale polycrystalline silicon MEMS structures," *J. Microelectromech. Syst.*, vol. 20, no. 4, pp. 922–932, Aug. 2011.
[37] H. Kahn, N. Tayebi, R. Ballarini, M. L. Mullen, and A. H. Heuer, "Fracture toughness of polysilicon MEMS devices," *Sens. Actuators A, Phys.*, vol. 82, no. 1–3, pp. 274–280, May 2000.
[38] I. Chasiotis, S. W. Cho, and K. Jonnalagadda, "Fracture toughness and subcritical crack growth in polycrystalline silicon," *J. Appl. Mech.*, vol. 73, no. 5, pp. 714–722, 2006.
[39] M. T. Todinov, "Probability of fracture initiated by defects," *Mater. Sci. Eng. A*, vol. 276, no. 1–2, pp. 39–47, Jan. 2000.

Michael S. Gaither received the B.S. degree in physics from Austin Peay State University, Clarksville, TN, in 2006 and the Ph.D. degree in materials science and engineering from the University of Maryland, College Park, in 2011.

From 2007 to 2012, he was with the National Institute of Standards and Technology, Gaithersburg, MD, first as a Graduate Student Researcher (2007–2011) and then as a National Research Council Postdoctoral Researcher (2011–2012), both with the Nanomechanical Properties Group. His research interests include microscale mechanical properties measurement and fracture.

Richard S. Gates received the B.S. degree in chemistry from Hobart College, Geneva, NY, in 1978. He received the M.S. degree in chemical engineering from The Pennsylvania State University, University Park, in 1987 based on his research on the tribochemical mechanism of aluminum oxide with water. In 1993, he received the Ph.D. degree in chemical engineering from The Pennsylvania State University based on his discovery of the boundary lubrication mechanism of silicon nitride ceramics with alcohols.

He began his research career studying lubricant chemistry in the Recycled Oil Program with the National Bureau of Standards (NBS), Gaithersburg, MD, in 1978. His research continued in tribology with an emphasis on tribochemistry, as NBS transitioned into the National Institute of Standards and Technology (NIST) in 1988. He is currently the Group Leader of the Nanomechanical Properties Group with the Material Measurement Laboratory, NIST. Most recently, his research interests have focused on issues related to nanotribology and measurement of material properties at the nanoscale with an emphasis on nanomechanical measurement calibration, particularly for atomic force microscopy.

Dr. Gates is a member of the American Chemical Society and the Society of Tribologists and Lubrication Engineers.

Rebecca Kirkpatrick received the B.S. degree in materials science and engineering and the B.A. degree in Asian studies from Lehigh University, Bethlehem, PA, in 2001 and the M.S. and Ph.D. degrees in materials science and engineering from The Pennsylvania State University, University Park, in 2005 and 2010, respectively.

From 2008 to 2010, she was with the National Institute of Standards and Technology (NIST), Gaithersburg, MD. She is currently with the The Pennsylvania State University as a Postdoctoral Researcher. She is also with the Nanomechanical Properties Group, Ceramics Division, NIST. Her research interests include micro- and nanoscale mechanical evaluation and reliability, with a focus on statistical analysis.

Robert F. Cook received the B.Sc. degree (Hons.) in physics from Monash University, Melbourne, Australia, in 1981 and the Ph.D. degree in physics from the University of New South Wales, Sydney, Australia, in 1986.

In 1982 and 1984, he was a Guest Researcher with the National Institute of Standards and Technology (NIST, then known as the National Bureau of Standards), Gaithersburg, MD. In 1985, he joined the Physical Sciences Department, IBM Research, Yorktown Heights, NY, first as a Postdoctoral Researcher and then as a Research Staff Member, and for a time, as a Senior Manager. From 1998 to 2004, he was a Professor of materials science and engineering with the University of Minnesota, Minneapolis. In 2005, he was a Senior Scientist with the University of Maryland, College Park. In 2006, he joined NIST as the Leader of the Nanomechanical Properties Group and the Deputy Chief of the Ceramics Division within the Materials Science and Engineering Laboratory. In 2011, he was promoted to the position of NIST Fellow within the newly formed Material Measurement Laboratory. He has authored over 160 peer-reviewed publications and is a holder of 14 patents. His research interests are in mechanics and mechanical properties of materials, particularly fracture.

Dr. Cook is a Fellow of the American Ceramic Society. He was a recipient of a U.S. Department of Commerce Silver Medal in 2008 for Scientific/Engineering Achievement for his role in the development of the first gold nanoparticle reference materials for biomedical applications. In 2011, he received a U.S. Department of Commerce Bronze Medal for the development of a scanning probe technique for simultaneous measurement of mechanical and electrical properties of molecular films.

Frank W. DelRio received the B.S. degree in mechanical engineering from Carnegie Mellon University, Pittsburgh, PA, in 1998, the M.S. degree in mechanical engineering from Boise State University, Boise, ID, in 2002, and the Ph.D. degree in mechanical engineering from the University of Colorado, Boulder, in 2006.

After receiving the B.S. degree, he worked as a Product Support Engineer with C&D Aerospace (now C&D Zodiac), first in Huntington Beach, CA, and later in São José dos Campos, Brazil. In 2001, he returned to academia. During his tenure at the University of Colorado, he served as a Microsystems and Engineering Sciences Applications Institute Fellow with Sandia National Laboratories in Albuquerque, NM, and as an Engineering Sciences Summer Institute Fellow with Sandia National Laboratories in Livermore, CA. After working as a Postdoctoral Researcher with the Department of Chemical Engineering, University of California, Berkeley, he joined the Materials Science and Engineering Laboratory (now the Material Measurement Laboratory), National Institute of Standards and Technology, Gaithersburg, MD, as the Leader for the Nanoscale Strength Measurements and Standards project. In all, he has authored or coauthored close to 30 peer-reviewed papers and five book chapters on topics related to the fabrication of micro- and nanoscale ceramic; metallic, polymeric, and composite thin films; and small-scale structures and the characterization of their elastic, plastic, fracture, interfacial, and charge transport properties.

Dr. DelRio has been recognized with several awards and honors, including the American Society of Mechanical Engineers Orr Early Career Award; the Minerals, Metals & Materials Society Young Leader Professional Development Award; the Department of Commerce Bronze Medal Award; the Adhesion Society Outstanding Young Adhesion Scientist Award; and the Presidential Early Career Award for Scientists and Engineers.